

# Captured are circularized: A relativistic treatment of extreme mass ratio inspirals crossing accretion disks

Yuhe Zeng<sup>1,2,\*</sup> and Zhen Pan<sup>1,2,†</sup>

<sup>1</sup>*Tsung-Dao Lee Institute, Shanghai Jiao-Tong University, Shanghai, 520 Shengrong Road, 201210, People's Republic of China*

<sup>2</sup>*School of Physics & Astronomy, Shanghai Jiao-Tong University, Shanghai, 800 Dongchuan Road, 200240, People's Republic of China*

(Dated: January 21, 2026)

A small body orbiting around an accreting massive object and periodically crossing its accretion disk is a common configuration in astrophysics. In this work, we investigate the secular evolution of extreme mass-ratio inspirals (EMRIs), in which a stellar-mass object (SMO), e.g., a star or a stellar-mass black hole (sBH), collides with the accretion disk of a central supermassive black hole (SMBH), within a fully relativistic framework. We find (1) the disk always tends to align the SMO no matter what the initial orbital inclination  $i$  relative to the disk is, (2) the final orbital eccentricity of the SMO captured by the disk is always low though the orbital eccentricity may temporarily grow when the orbital inclination  $i$  is large and the SMO is an sBH, and (3) via collisions with the accretion disk only, only a small fraction of sBHs that are initially close to the SMBH and close to the disk can be captured by the disk within typical disk lifetime of active galactic nuclei. Two-body scatterings between SMOs in the nuclear stellar cluster play an essential role in randomly kicking sBHs towards the disk and boosting the capture rate.

## I. INTRODUCTION

Astrophysical systems in which a small body orbits around an accreting massive central object appear in a wide range of environments, e.g., (i) planetesimals interacting with circumstellar material around white dwarfs (WDs) or young planets embedded in protoplanetary disks, where gas drag or disk–planet torques drive orbital migration and damp eccentricity and inclination [1–3]; (ii) compact stellar-mass objects (SMOs) or stars interacting with the dense gas of active galactic nucleus (AGN) disks, which can trap, align and migrate small objects and facilitate hierarchical mergers [4–9]; (iii) SMOs around supermassive black holes (SMBHs) interacting with transient accretion disks formed in tidal disruption events (TDEs) and producing X-ray quasi-periodic eruptions (QPEs) [10–16]. Together, these systems provide a unified physical setting in which an orbiting secondary interacts with the central massive object itself or with its ambient environment, leading to secular modifications of the orbit and distinctive radiative signatures. A substantial body of work has focused on how such interactions drive the secular evolution of orbiting secondaries. Depending on the environment, long-term orbital changes may arise from gravitational radiation, dissipative gas torques, dynamical friction [17, 18], or impulsive perturbations during disk crossings [1, 18–24]. Over timescales much longer than the orbital period, the small effects produced by these forces accumulate into a net secular drift of the orbital elements, corresponding to the usual adiabatic evolution of the system.

One class of such astrophysical systems, extreme mass-ratio inspiral (EMRI), typically consisting of a central SMBH and an orbiting SMO, which can be a stellar companion or

a compact remnant such as a stellar-mass black hole (sBH), satisfying a mass ratio  $q \equiv m_{\text{SMO}}/M_{\text{SMBH}} \lesssim 10^{-4}$ , is among the primary gravitational-wave sources targeted by the future space-based mission LISA [25], TianQin [26] and Taiji [27]. Their long-lived, relativistic dynamics encode detailed information about the strong-field spacetime and thereby enable precision tests of general relativity (GR) and measurements of SMBH properties [28–30]. Although EMRIs are often treated as vacuum systems, realistic AGNs contain dense stellar clusters and accretion disks, within which compact objects may reside or migrate [7, 31–36]. In such environments, SMOs in EMRIs may experience non-negligible matter-induced forces, including aerodynamic drag, hydrodynamical torques, and gas dynamical friction, all of which may significantly modify their orbital evolution relative to vacuum inspirals. Such systems, often termed “wet EMRIs” [33], can deviate in both secular orbital-parameter evolution and inspiral timescales, affecting not only the astrophysical interpretation of their dynamics but also the accuracy of waveform templates required for LISA data analysis [37–39].

Formation of wet EMRIs in AGN disks by capturing SMOs on misaligned orbits has been investigated in detail [35]. Two-body scatterings randomly kick SMOs onto low-inclination orbits, and density waves excited by low-inclination SMOs along with dynamical friction efficiently capture the SMOs onto the AGN disk. Density waves drive the SMOs to migrate inward as well as damping their orbital eccentricities [40, 41]. As a result, wet EMRIs in the LISA sensitivity band are expected to be of low eccentricity. On the other hand, there are also recent studies [42, 43] of eccentric wet EMRIs and their scientific potentials motivated by previous studies showing that SMO-disk collisions may increase the orbital eccentricity in some parameter space [19, 23].

In this work, we investigate the orbital evolution of induced by SMO-disk collisions within a fully relativistic framework. Specifically, we model the motion of the SMO as a forced geodesic in the Schwarzschild spacetime and consider its re-

\* [zengyuhe@sjtu.edu.cn](mailto:zengyuhe@sjtu.edu.cn)

† [zhpan@sjtu.edu.cn](mailto:zhpan@sjtu.edu.cn)

peated crossings of a geometrically thin accretion disk located on the equatorial plane. To quantify the secular evolution of the orbit, we derive the equations governing the variations of the principal orbital elements  $a$ ,  $e$ , and  $\iota$  (see Fig. 1), directly with respect to the proper time  $\tau$ . By applying an adiabatic approximation procedure over the fast orbital phases, we extract the net secular evolution driven by SMO-disk collisions and determine the associated characteristic timescales for orbital shrinkage, inclination damping, and also the tendency of eccentricity evolution.

This paper is organized as follows. In Sec. II, we introduce the evolution equations for the orbital elements, the adiabatic orbit-averaging scheme used to obtain their secular behavior, and also summarizes the two force models considered in this work. In Sec. III, we present the secular evolution of the orbital parameters under the two force models and derives the scaling relations that govern the characteristic timescales, and compare our findings with previous studies, extend the timescale estimates using the adopted disk model and scaling relations. We conclude this work with Sec. III C. In Appendices A, B, and C, we provide details of the key formulae used in this work. Throughout this work, we use geometrical units with  $G = c = 1$ .

## II. BASIC FRAMEWORK

### A. Forced EMRI motion around a SMBH

Within the GR framework, the motion of a freely falling test particle is simply described by a geodesic of the background spacetime. However, the geodesic motion is perturbed by external forces in non-vacuum environments and the equation of motion (E.O.M.) is written as

$$\frac{d^2 x^\mu}{d\tau^2} + \Gamma_{\alpha\beta}^\mu \frac{dx^\alpha}{d\tau} \frac{dx^\beta}{d\tau} = f^\mu, \quad (1)$$

where  $x^\mu$  is the four-coordinate of the SMO around the central SMBH, and  $f^\mu$ ,  $\tau$  denote the four-acceleration and proper time, respectively. In the vacuum environment, the external force vanishes,  $f^\mu = 0$ . The form of  $f^\mu$  in the reference of the zero-angular-momentum observers (ZAMOs) has been given in Ref. [44],  $f^\mu$  was assumed to depend linearly on the spatially projected component of the relative four-velocity  $u_\perp^\mu$ , and in order to enforce the orthogonality condition, additional correction terms associated with  $u_{\text{ZAMO}}^\mu$  was also included, thus,

$$f^\mu = -\gamma u_\perp^\mu + \kappa u_{\text{ZAMO}}^\mu, \quad (2)$$

where  $u_\perp^\mu = u^\mu + \Gamma u_{\text{ZAMO}}^\mu$  with  $\Gamma \equiv u_{\text{ZAMO}}^\mu u_\mu$ , and with the constraints of  $u^\mu u_\mu = -1$  and equivalently,  $f^\mu u_\mu = 0$ , there is  $\kappa = \gamma(\Gamma - 1/\Gamma)$ , then

$$\begin{aligned} f^\mu &= -\gamma u_\perp^\mu + \gamma \left( \Gamma - \frac{1}{\Gamma} \right) u_{\text{ZAMO}}^\mu \\ &= -\gamma \left( u^\mu + \frac{u_{\text{ZAMO}}^\mu}{u_{\text{ZAMO}} \cdot u^t} \right), \end{aligned} \quad (3)$$

with the four velocity of the ZAMOs satisfying  $u_{\text{ZAMO}} \cdot \phi = 0$ . Here  $\gamma$  denotes the interaction (damping) coefficient that encodes the strength of the force exerted on the SMO. When combined with the relative velocity between the SMO and the ZAMO frame, it determines the individual components of the resulting four-acceleration.

In the case of an SMO interacting with an accretion disk, the disk is assumed to follow nearly Keplerian rotation around the central SMBH and to be geometrically thin. The force exerted on the SMO therefore depends not only on the local disk properties but also on the relative velocity between the SMO and the disk material. In this work, we incorporate both the spatial dependence of the interaction coefficients and the actual relative velocity determined by the Keplerian motion of the disk material within the thin-disk approximation. Starting from the density profile of the disk, we adopt an axisymmetric configuration in which the thin-disk density distribution is expressed as a function of the radial coordinate  $r$  and the polar angle  $\theta$ , assuming a Gaussian density profile in the vertical direction:

$$\rho_{\text{gas}}(r, \theta) = \rho_g \exp \left[ -\frac{(\theta - \pi/2)^2}{2(H_{\text{disk}}/r)^2} \right], \quad (4)$$

where  $\rho_g$  is the reference density of the disk and  $H_{\text{disk}}$  denotes the disk scale height to the midplane. This distribution effectively confines the disk material to the vicinity of the equatorial plane when  $H_{\text{disk}} \ll r$ . Consequently, in our calculations the SMO interacts significantly with the gas only when it passes near the midplane. Moreover, since the present analysis is restricted to a finite radial interval and aims to isolate the dynamical impact of disk crossings rather than to model the global disk structure, we omit any additional radial dependence beyond the exponential angular profile introduced above. Under the thin-disk approximation, the disk matter is confined to  $\theta = \pi/2$ , and the corresponding four-velocity components are

$$\begin{aligned} u_{\text{disk}}^r &= u_{\text{disk}}^\theta = 0, \\ g_{\mu\nu} u_{\text{disk}}^\mu u_{\text{disk}}^\nu &= -1, \\ u_{\text{disk}}^\phi &= \Omega_K u_{\text{disk}}^t, \end{aligned} \quad (5)$$

where

$$\Omega_K^\pm = \pm \frac{\sqrt{M_\bullet}}{r^{3/2} \pm a_\bullet \sqrt{M_\bullet}} \quad (6)$$

denotes the Keplerian angular velocity in the Kerr spacetime with  $a_\bullet$  the spin parameter of the central SMBH. The “+” branch corresponds to prograde rotation, i.e., the angle between the disk angular momentum and the SMBH spin is less than  $90^\circ$ , whereas the “-” branch corresponds to retrograde rotation. In the present work, which is carried out in the Schwarzschild spacetime, the sign is determined by the vertical projection of the orbital angular momentum of the SMO onto the SMBH spin direction. By substituting  $u_{\text{ZAMO}}^\mu$  in Eq. (3) with  $u_{\text{disk}}^\mu$ , the four-acceleration for the SMO-disk collision scenario is derived, with the  $r$ ,  $\theta$ ,  $\phi$  components presented in Appendix A.

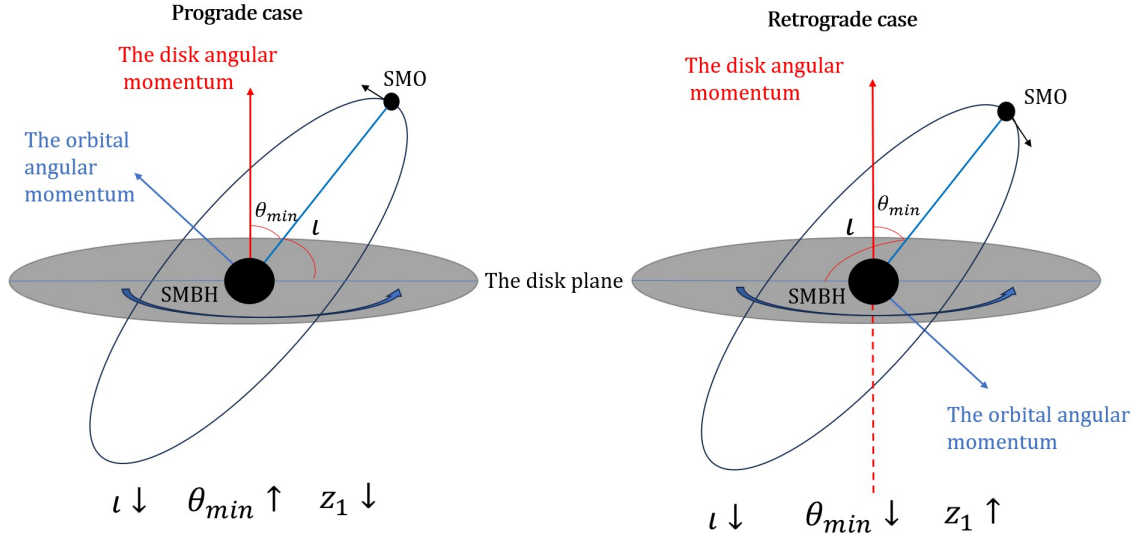


FIG. 1. Schematic illustration of the wet EMRIs with SMO-disk collision scenario. The relations between the labeled parameters are  $z_1 \equiv \cos \theta_{\min} = \sin i$ , where  $\vec{L}_{\text{disk}}$  is the disk angular momentum, and  $\vec{L}_{\text{orbit}}$  is the orbital angular momentum of the SMO, the angle between these two vectors is equivalent to the orbital inclination,  $\cos^{-1}(\vec{L}_{\text{disk}} \cdot \vec{L}_{\text{orbit}}) = i$ .  $0 < i < 90^\circ$  corresponds to the prograde cases, while  $90^\circ < i < 180^\circ$  corresponds to the retrograde cases. In both cases  $i$  will decrease, which will be verified in this work.

## B. Damping coefficient $\gamma$

In this subsection, we compute the damping coefficient  $\gamma$  in Eq. (3) for both star-disk collisions and sBH-disk collisions. The coefficient  $\gamma$  depends on several factors, including the interaction type, the size of the SMO, the gas density and scale height of the disk.

According to the thin-disk density profile in Eq. (4), the effects of SMO-disk collisions are strongly localized near the equatorial plane,  $\theta = \pi/2$ . In this region, where  $|\theta - \pi/2| \ll 1$ , one may approximate  $r^2(\theta - \pi/2)^2/H_{\text{disk}}^2 \approx r^2 \cos^2 \theta / H_{\text{disk}}^2$ . In terms of disk surface density  $\Sigma_g$  and disk height to the mid-plane  $H_{\text{disk}}$ , the reference gas density  $\rho_g$  in Eq. (4) is estimated by treating the thin disk as having an effective vertical thickness  $2H_{\text{disk}}$  and a uniform density within this narrow region as  $\rho_g \approx \Sigma_g / 2H_{\text{disk}}$ . The damping coefficient is then formulated as

$$\gamma(r, \theta) = \gamma_g \exp \left[ -\frac{(\theta - \pi/2)^2}{2(H_{\text{disk}}/r)^2} \right], \quad (7)$$

where  $\gamma_g$  is the reference damping coefficient apart from the spatial-distribution dependence.

For star-disk collisions, the perturbation force is dominated by aero-drag force [19]

$$\mathbf{F}_{\text{aero}} = -\pi R_{\star}^2 \rho_g v_{\text{rel}} \mathbf{v}_{\text{rel}}, \quad (8)$$

where  $\mathbf{v}_{\text{rel}} \equiv \mathbf{v} - \mathbf{v}_g$  denotes the relative velocity between the star and the local gas in the disk,  $v_{\text{rel}} \equiv |\mathbf{v}_{\text{rel}}|$ ,  $R_{\star}$  is the stellar radius and  $\rho_g$  is the gas density of the disk. Consequently, the reference damping coefficient  $\gamma_g$  can be written in the numer-

ical form as

$$\begin{aligned} \gamma_g &= \pi R_{\star}^2 \rho_g v_{\text{rel}} m_{\star}^{-1} \\ &= 2.55 \times 10^{-8} \left( \frac{R_{\star}}{R_{\odot}} \right)^2 \left( \frac{m_{\star}}{M_{\odot}} \right)^{-1} \\ &\quad \cdot \left( \frac{v_{\text{rel}}}{0.1c} \right) \left( \frac{\rho_g}{10^5 \text{ g} \cdot \text{cm}^{-2} / 3M_{\bullet}} \right) [M_{\bullet}^{-1}]. \end{aligned} \quad (9)$$

For sBH-disk collisions, the effective radius of an sBH with mass  $m_{\bullet}$  is given by its horizon radius  $R_H = 2m_{\bullet}$ , which is much smaller than that of a stellar object with the same mass, and the perturbation force is dominated by dynamical friction [19, 45]

$$\mathbf{F}_{\text{dyn}} = -\mathcal{I} \frac{4\pi(Gm_{\bullet})^2 \rho_g}{v_{\text{rel}}^3} \mathbf{v}_{\text{rel}}, \quad (10)$$

where the coefficient  $\mathcal{I}$  is related with Mach number  $\mathcal{M} \equiv v_{\text{rel}}/c_s$ . In this work, we note that  $\mathcal{I} \sim \mathcal{O}(1)$  in the relevant parameter regime and mainly rescales the interaction strength. We therefore set  $\mathcal{I} = 1$ , for simplicity, which does not affect the qualitative orbital-evolution behavior discussed below. The reference damping coefficient  $\gamma_g$  associated with the acceleration dominated by dynamical friction can be written in the numerical form as

$$\begin{aligned} \gamma_g &\approx \frac{4\pi G^2 m_{\bullet} \rho_g}{v_{\text{rel}}^3} \\ &= 4.62 \times 10^{-15} \left( \frac{m_{\bullet}}{M_{\odot}} \right) \left( \frac{v_{\text{rel}}}{0.1c} \right)^{-3} \left( \frac{\rho_g}{10^5 \text{ g} \cdot \text{cm}^{-2} / 3M_{\bullet}} \right) [M_{\bullet}^{-1}]. \end{aligned} \quad (11)$$

For clarity, the reference damping coefficient  $\gamma_g$  is expressed as the combination of a constant baseline value  $\gamma_0$  and

a velocity-dependent contribution arising from the relative motion. Specifically, for aero-drag force,  $\gamma_g = \gamma_0 (v_{\text{rel}}/0.1 c)$ , whereas for dynamical friction,  $\gamma_g = \gamma_0 (v_{\text{rel}}/0.1 c)^{-3}$ . The relative velocity is computed from

$$v_{\text{rel}} = \sqrt{1 - \frac{1}{(u_\mu u^\mu_{\text{disk}})^2}}. \quad (12)$$

### C. Orbital Evolution: Osculating orbit

There are effectively seven degrees of freedom in the orbital dynamics of an SMO in curved spacetime: four coordinate components and four velocity components subject to one normalization constraint  $u^\alpha u_\alpha = -1$ . To parameterize this motion, we introduce a set of five orbital elements, corresponding to the degrees of freedom beyond the  $t$  and  $\phi$  coordinates, denoted by the conserved parameter set  $\mathbf{I} = \{p, e, z_1\}$ , and phases  $\psi_r, \psi_\theta$ . These parameters are related to the radial and polar motions in Boyer–Lindquist coordinates through

$$\begin{aligned} r &= \frac{p}{1 + e \cos \psi_r}, \\ \cos \theta &= z_1 \cos \psi_\theta. \end{aligned} \quad (13)$$

Here,  $p$  is the semi-latus rectum,  $e$  is the eccentricity, and  $z_1 \equiv \cos \theta_{\text{min}}$ , the angle  $\theta_{\text{min}}$  is related to the orbital inclination  $\iota$  with respect to the disk plane via  $\theta_{\text{min}} = \pi/2 - \iota$ . The range  $0 < \iota < 90^\circ$  corresponds to prograde orbits, whereas  $90^\circ < \iota < 180^\circ$  corresponds to retrograde orbits.  $\psi_r$  and  $\psi_\theta$  represent the phase variables associated with the radial and polar motions, respectively.

For simplicity, we consider a Schwarzschild SMBH of mass  $M_\bullet$  in this work. The spacetime metric is

$$ds^2 = -\left(1 - \frac{2M_\bullet}{r}\right)dt^2 + \left(1 - \frac{2M_\bullet}{r}\right)^{-1}dr^2 + r^2(d\theta^2 + \sin^2 \theta d\phi^2). \quad (14)$$

Owing to the spherical symmetry of the Schwarzschild background, for spherically symmetric perturbations, the polar parameter  $z_1$  remains constant, and the orbital plane may be chosen as the equatorial plane without loss of generality, leaving only a single radial phase parameter  $\psi_r$  to characterize the motion. However, in the SMO-disk collision scenario, the breaking of spherical symmetry by the existence of equatorial disk requires an additional polar phase parameter  $\psi_\theta$  to fully characterize the orbital evolution.

Following Ref. [46], the equations of motion of a test particle around a Schwarzschild black hole are written as

$$\begin{aligned} \left(\frac{dr}{d\tau}\right)^2 &= E^2 - \left(1 - \frac{2M_\bullet}{r}\right)\left(1 + \frac{J^2}{r^2} \cdot \frac{1}{1 - z_1^2}\right), \\ \left(\frac{d\theta}{d\tau}\right)^2 &= \frac{J^2}{r^4 \sin^2 \theta} \cdot \frac{1}{1 - z_1^2} \cdot (z_1^2 - \cos^2 \theta), \\ \frac{dt}{d\tau} &= E \left(1 - \frac{2M_\bullet}{r}\right)^{-1}, \\ \frac{d\phi}{d\tau} &= \frac{J}{r^2} \cdot \frac{1}{1 - \cos^2 \theta}, \end{aligned} \quad (15)$$

where  $E, J$  are the conservation quantities, energy and angular momentum respectively. In the following derivations, we set  $M_\bullet = 1$  for simplicity.

Based on Eqs. (15), the frequencies of the unperturbed geodesic motion for phases  $\psi_r, \psi_\theta$  can be obtained as

$$\begin{aligned} \frac{d\psi_r}{d\tau} &:= \omega_r = \frac{1}{(\partial r / \partial \psi_r)} \frac{dr}{d\tau} = (1 + e \cos \psi_r)^2 \sqrt{\frac{p - 6 - 2e \cos \psi_r}{p^3(p - 3 - e^2)}}, \\ \frac{d\psi_\theta}{d\tau} &:= \omega_\theta = \frac{1}{(\partial \theta / \partial \psi_\theta)} \frac{d\theta}{d\tau} = \frac{(1 + e \cos \psi_r)^2}{p \sqrt{p - 3 - e^2}}. \end{aligned} \quad (16)$$

Notice that  $\omega_\theta$  depends solely on  $\psi_r$ . By integrating  $\frac{d\psi_\theta}{d\psi_r} = \omega_\theta / \omega_r$ , the relation between two phases is found as

$$\psi_\theta(\psi_r) = 2 \sqrt{\frac{p}{p - 6 - 2e}} F\left(\frac{\psi_r}{2} \mid \frac{4e}{6 + 2e - p}\right) + \psi_\theta \text{ini}, \quad (17)$$

where the function  $F$  is the incomplete elliptic integral of the first kind,

$$F(\phi \mid m) = \int_0^\phi \frac{d\theta}{\sqrt{1 - m \sin^2 \theta}}. \quad (18)$$

The forced motion of an SMO can be obtained by directly evolving the E.O.M. (Eq. (1)). Then the orbital parameters  $p, e, z_1$  can be extracted by inverting Eqs. (15) [46]. However, as the evolution timescale increases far exceeding the orbital period, the computational cost and the difficulty of precision control for such method rise rapidly, limiting the applicability to long-time evolution problems.

This motivates the development of faster evolution methods that average over the rapid oscillations on the orbital timescale and focus on the secular evolution of the orbital parameters, which can be divided into two main steps. First, the E.O.M. is reformulated in terms of orbital elements  $\{p, e, z_1, \psi_r, \psi_\theta\}$  using the method of osculating orbit. Second, applying the adiabatic approximation to the reformulated E.O.M. and extracting secular evolution of orbital elements as in the following Sec. II D.

Following Refs. [44, 47], the osculation condition can be written as

$$\begin{aligned} x^\mu(\tau) &= x_G^\mu[\tau, I_0(\tau)], \\ \frac{dx^\mu}{d\tau} &= \frac{\partial x_G^\mu}{\partial \tau}[\tau, I_0(\tau)], \end{aligned} \quad (19)$$

where  $x_G^\mu$  is the geodesic with orbital parameter set  $I_0 = \{p, e, z_1, \psi_0, \chi_0\}$ . Here  $\psi_0$  and  $\chi_0$  are the “initial” values of  $\psi_r$  and  $\psi_\theta$ , respectively. With definition  $\psi_r = \psi - \psi_0$  one can decompose the phase evolution in the radial direction as a geodesic part  $\psi$  governed by Eqs. (16), and a perturbation induced shift in the “initial” phase  $\psi_0$ . In the same way, the phase evolution in the polar direction is decomposed as two parts,  $\psi_\theta = \chi - \chi_0$ . Defined in this way, parameters  $I_0$  remain conserved for unperturbed geodesic motion, however, in the presence of perturbations, it undergoes a slow secular drift superposed with oscillatory variations on the orbital timescale.

With the osculation condition, one can reformulate the E.O.M. (1) in terms of parameters  $I_0$ . At each instant  $\tau$ , the worldline is treated as a geodesic tangent to the true trajectory, with instantaneous orbital element set  $I_0(\tau)$ . Considering 4-velocity  $u^\mu$  along with the 1st osculation condition in Eq. (19), one can find [47]

$$u^\mu := \frac{dx_G^\mu}{d\tau} = \frac{\partial x_G^\mu}{\partial \tau} + \frac{\partial x_G^\mu}{\partial I_0^a} \frac{dI_0^a}{d\tau} = \frac{dx_G^\mu}{d\tau}, \quad (20)$$

which in combination with the 2nd osculation condition in Eq. (19) immediately leads to

$$\frac{\partial x_G^\mu}{\partial I_0^a} \frac{dI_0^a}{d\tau} = 0. \quad (21)$$

Considering 4-acceleration  $du^\mu/d\tau$  along with Eqs. (20,21) and the geodesic definition of  $x_G^\mu$

$$\frac{\partial^2 x_G^\mu}{\partial \tau^2} + \Gamma_{\alpha\beta}^\mu \frac{\partial x_G^\alpha}{\partial \tau} \frac{\partial x_G^\beta}{\partial \tau} = 0, \quad (22)$$

the E.O.M. (1) can be rewritten as

$$\frac{d^2 x^\mu}{d\tau^2} = -\Gamma_{\alpha\beta}^\mu u^\alpha u^\beta + f^\mu = \frac{\partial^2 x_G^\mu}{\partial \tau^2} + f^\mu. \quad (23)$$

On the other hand, the same quantity can also be expressed as

$$\frac{d^2 x^\mu}{d\tau^2} = \frac{\partial^2 x_G^\mu}{\partial \tau^2} + \frac{\partial}{\partial I_0^a} \left( \frac{dx_G^\mu}{d\tau} \right) \frac{dI_0^a}{d\tau}, \quad (24)$$

using Eqs. (19) and (21). With Eq. (23) and (24), the forced E.O.M. (1) can be written as

$$\frac{\partial}{\partial I_0^a} \left( \frac{dx_G^\mu}{d\tau} \right) \frac{dI_0^a}{d\tau} = f^\mu. \quad (25)$$

The final step is to isolate individual components  $dI_0^a/d\tau$  from Eqs. (21) and (25), which contains eight equations. By imposing the orthogonality condition  $f^\mu u_\mu = 0$ , and evolving  $t$  and  $\phi$  explicitly using the geodesic expressions evaluated along the instantaneous orbit [44], three equation components, i.e.,  $\mu = t, \phi$  components of Eq. (21) and  $\mu = t$  component of Eq. (25), can be removed. As a result, the evolution of the five orbital parameters with respect to  $\tau$  can be written generally as

$$\frac{dI_0}{d\tau} = C_r^{(I_0)} f^r + C_\theta^{(I_0)} f^\theta + C_\phi^{(I_0)} f^\phi, \quad (26)$$

with the detailed expressions of coefficients  $C_{r,\theta,\phi}^{(I_0)}$  shown in Appendix. B.

#### D. Secular evolution

In systems subject to weak perturbations, the orbital motion is well approximated by a geodesic on short timescales,

while the perturbations accumulate over many orbital periods and induce a slow secular evolution of the orbital parameters. Such separation between the short orbital period and the long inspiral timescale justifies the use of the adiabatic approximation. For star-disk collisions considered in this work, the SMO interacts with the thin disk twice per orbital period, and each encounter produces a small perturbation, allowing this method to reliably determine the secular evolution.

Consider a perturbed system characterized by  $N$  phases  $\psi = \{\psi_1, \psi_2, \dots, \psi_N\}$  and a set of orbital parameters  $\mathbf{I} = \{I_1, I_2, \dots, I_M\}$  that would remain conserved in the absence of perturbations. For a function  $f = f(\psi, \mathbf{I})$ , if the unperturbed frequencies associated with each  $\psi_j$  depend only on that phase, namely  $\omega_j = \omega_j(\psi_j, \mathbf{I})$ , and if each  $\psi_j$  is assumed to have a period of  $2\pi$ , then the adiabatic approximation of  $f(\psi, \mathbf{I})$  can be evaluated as [44]

$$\langle f \rangle_{\mathbf{I}} = \frac{\int_0^{2\pi} d\psi \prod_{j=1}^N \frac{1}{\omega_j(\psi_j, \mathbf{I})} f(\psi, \mathbf{I})}{\prod_{j=1}^N \int_0^{2\pi} d\psi_j \frac{1}{\omega_j(\psi_j, \mathbf{I})}}, \quad (27)$$

where the numerator on the right-hand side denotes the  $N$ -dimensional integral over the phase set  $\psi$ . It has been noted in Ref. [44] that for more general systems in which  $\omega_j = \omega_j(\psi, \mathbf{I})$ , the adiabatic approximation may not take the form of Eq. (27).

In Schwarzschild spacetime, both frequencies in Eqs. (16) solely depend on phase  $\psi_r$ . This corresponds to a special case in which the adiabatic average can still be evaluated in a form analogous to Eq. (27) as

$$\langle f \rangle_{\mathbf{I}} = \frac{\int_0^{2\pi} d\psi_\theta \int_0^{2\pi} d\psi_r \frac{1}{\omega_r(\psi_r, \mathbf{I})} f(\psi_r, \psi_\theta, \mathbf{I})}{2\pi \int_0^{2\pi} d\psi_r \frac{1}{\omega_r(\psi_r, \mathbf{I})}}, \quad (28)$$

note that the integration is carried out over the periodic domains of both  $\psi_r$  and  $\psi_\theta$ , while only the  $\omega_r$  appears in the denominator of the integrand. The equivalent form adopted in this work is shown in Appendix. C. The adiabatic E.O.M. is obtained by applying the average above to both sides of Eq. (26),

$$\frac{d\langle I_0 \rangle}{d\tau} = \left\langle C_r^{(I_0)} f^r + C_\theta^{(I_0)} f^\theta + C_\phi^{(I_0)} f^\phi \right\rangle, \quad (29)$$

where  $\langle C_i^{(I_0)} f^i \rangle$  on the right hand side can be precomputed for the purpose of numerical efficiency.

## III. RESULTS

### A. Orbital evolution of stars

To assess the reliability of the adiabatic approximation in tracking secular evolution of a star colliding with an accretion disk, we first compare adiabatic evolution with full orbital evolution with the aero-drag force (8): the semi-major axis  $a(t) \equiv p/(1 - e^2)$ , the eccentricity  $e(t)$  and the inclination angle  $i(t)$ .

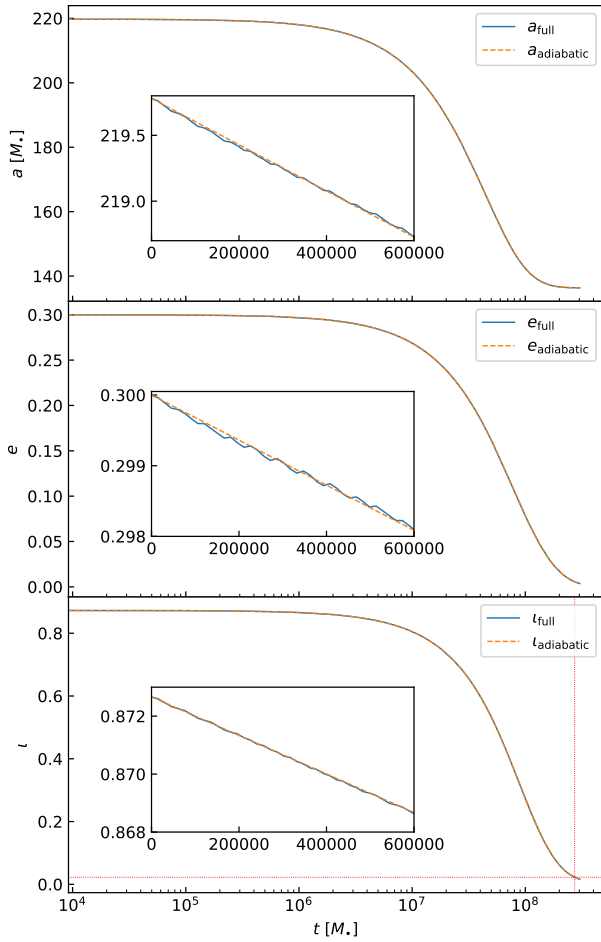


FIG. 2. Evolution of the semi-major axis  $a$ , eccentricity  $e$ , and orbital inclination angle  $\iota$  of star. Solid lines labeled “full” are obtained from full E.O.M. (1), while dashed lines labeled “adiabatic” show the secular evolution results obtained by evolving Eq. (29). The zoomed-in panels display the variations of  $a$ ,  $e$ ,  $\iota$  over the relatively short initial time interval  $(0, 6 \times 10^5 M_\bullet)$ . In the bottom panel, the intersection point of the two red dotted lines indicates the critical inclination  $\iota_{\text{crit}} = 3H_{\text{disk}}/p_{\text{ini}}$  and the corresponding time  $t_{\text{cap}} = 2.7 \times 10^8 M_\bullet$ .

As an example, we choose  $\gamma_0 = 2 \times 10^{-6} M_\bullet^{-1}$ , the initial conditions of the orbital parameters  $p_{\text{ini}} = 200 M_\bullet$ ,  $e_{\text{ini}} = 0.3$ ,  $\iota_{\text{ini}} = 50^\circ$ , and the initial phases  $\psi_0 \text{ ini} = 0$  and  $\chi_0 \text{ ini} = \pi/3$ . The disk height to the midplane is set to  $H_{\text{disk}} = 1.5 M_\bullet$ . As shown in Fig. 2, the adiabatic approximation works well in tracking secular evolution of the stellar orbit. The semi-major axis  $a$  decays over time due to energy loss caused by star-disk collisions. Note that  $a$  evolves slowly near the final stage when the star is close to be captured by the disk  $\iota \rightarrow H_{\text{disk}}/r$ , because their relative speed and the drag force are greatly reduced. The eccentricity  $e$  also decays with time and the orbit becomes nearly circular with a final value  $e_f = 3.6 \times 10^{-3}$  at the final stage of the evolution. Our numerical solution shows no secular evolution of the “initial” phases,  $\langle \dot{\psi}_0 \rangle = \langle \dot{\chi}_0 \rangle = 0$ , consistent with the expectation for the dissipative perturbing force as considered in this work [44].

For the purpose of illustrating the eccentricity evolution

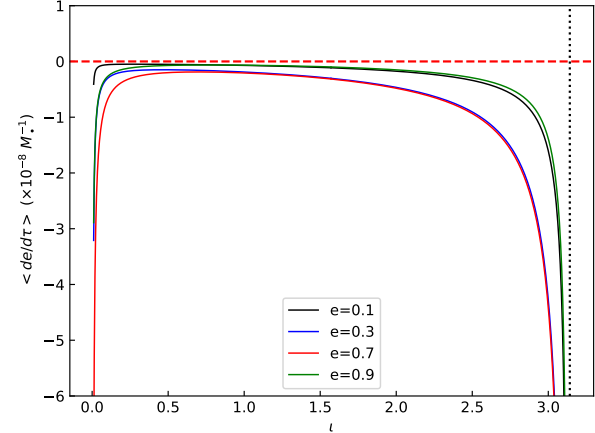


FIG. 3. The comparison of  $\langle de/d\tau \rangle$  variations with orbital inclination angle  $\iota$  for different  $e$ , with  $p_{\text{ini}} = 300 M_\bullet$  assuming the aero-drag force model. The vertical black dotted line marks  $\iota = \pi$  ( $180^\circ$ ).

driven by the aero-drag force, we compute the eccentricity evolution rate  $\langle de/d\tau \rangle$  as a function of the orbital inclination angle  $\iota$ , fixing the semi-latus rectum at  $p = 300 M_\bullet$  and considering representative eccentricity values  $e = 0.1, 0.3, 0.7, 0.9$ , as shown in Fig. 3. It is evident that star-disk collisions tend to circularize the star orbit for all inclination angles and orbital eccentricities.

To understand the final fate of a star colliding with a long-live disk, we compare the disk-capture timescale  $\tau_t := |\iota / \langle \frac{d\iota}{d\tau} \rangle_{\text{ini}}|$  and the orbital decay timescale  $\tau_a := |a / \langle \frac{da}{d\tau} \rangle_{\text{ini}}|$  associated with the shrinkage of the semi-major axis  $a$ , where

$$\left\langle \frac{da}{d\tau} \right\rangle = \left\langle \frac{1}{1 - e^2} \frac{dp}{d\tau} + \frac{2ep}{(1 - e^2)^2} \frac{de}{d\tau} \right\rangle. \quad (30)$$

As shown in Fig. 4, the capture timescale  $\tau_t$  increases with increasing  $\iota$ , whereas the orbital decay timescale  $\tau_a$  decreases due to the larger relative velocity between the star and the disk, which enhances the effect of the aero-drag force. As  $\iota \rightarrow 0$ , the timescale  $\tau_a$  also decreases, however, the star-disk collision model is no longer appropriate, since the orbit of the star becomes nearly embedded within the disk.

The comparison between  $\tau_t$  and  $\tau_a$  further shows that, for sufficiently large initial inclination angles, the orbital-decay timescale becomes shorter than the alignment timescale. This shows that a star on a high-inclination orbit will finally be disrupted by the central SMBH before being captured by the disk. On the other hand, a star on a low-inclination orbit will be captured by the disk before getting disrupted by the central SMBH. However, we note that in the actual orbital evolution, the semi-major axis and eccentricity evolve simultaneously, which can modify the rates of change of the parameters. Consequently, such estimates based solely on the initial values may not fully coincide with the true evolutionary behavior. The above calculations also show that  $\langle da/d\tau \rangle < 0$  and  $\langle de/d\tau \rangle < 0$  over the entire range of  $\iota$ , consistent with the

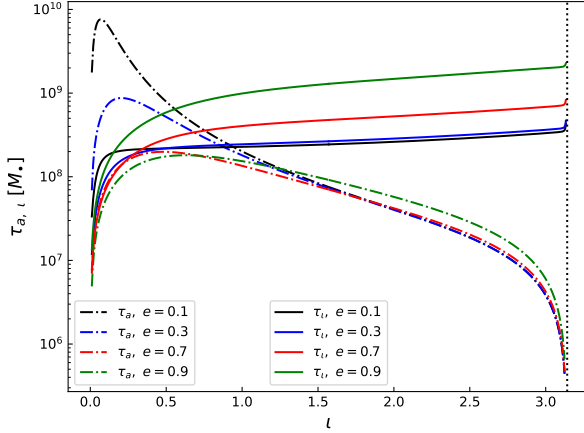


FIG. 4. The comparison of estimated shrink timescale with  $|a_{\text{ini}}/\langle \frac{da}{dt} \rangle_{\text{ini}}|$  (solid dotted line) and capture timescale with  $|\iota_{\text{ini}}/\langle \frac{d\iota}{dt} \rangle_{\text{ini}}|$  (solid line) with orbital inclination angle  $\iota$  for different  $e$ , fixing  $p_{\text{ini}} = 300 M_\star$ , using the aero-drag force model for stars. The vertical black dotted line marks  $\iota = \pi$  (180°).

expectation and with the actual evolution results found in this work.

After establishing the evolution behavior and the associated timescales for the orbital parameters  $a$ ,  $e$  and  $\iota$  under the aero-drag force, we now present several representative numerical examples of the orbital evolution computed within the adiabatic approximation. We consider orbits with an initial semi-latus rectum  $p_{\text{ini}} = 300 M_\star$  and compute the evolution with different initial inclination angles, focusing on initial eccentricities of  $e_{\text{ini}} = 0.3, 0.7$ , under the aero-drag force model with  $\gamma_0 = 2 \times 10^{-6} M_\star^{-1}$ . The evolution of  $a$ ,  $e$ ,  $\iota$  in the case of  $e_{\text{ini}} = 0.3$  with different initial inclination angles under the aero-drag force model is shown in the three panels of Fig. 5.

As shown in the top and bottom panels of Fig. 5, for the cases with  $\iota_{\text{ini}} \geq 130^\circ$ , the orbits shrink, with the semi-major axis  $a$  decreasing to below  $10 M_\star$ , before alignment with the disk plane is achieved. For the cases with  $\iota_{\text{ini}} \leq 110^\circ$ , the star successfully aligns with the disk plane and does not undergo significant shrinkage. The middle panel of Fig. 5 shows that the aero-drag force circularizes orbits with different inclination angles, regardless of the initial inclination. We also find that stars on low-inclination orbits require longer capture times. This is primarily because, for low-inclination orbits, the relative velocity between the SMO and the disk material is small. According to Eq. (8),  $|\mathbf{F}_{\text{aero}}| \propto |\mathbf{v}_{\text{rel}}|^2$ , leading to a correspondingly slower orbital evolution. In addition, during the alignment process, the semi-major axis  $a$  gradually decreases, which increases  $|\mathbf{v}_{\text{rel}}|$  and accelerates the subsequent evolution. This effect further explains why low-inclination stars experience longer capture times: although high-inclination orbits require larger changes in inclination, they initially evolve more rapidly due to their larger relative velocities, and the accompanying shrinkage of  $a$  during alignment further enhances this evolution, resulting in shorter capture times overall.

The evolution of  $a$ ,  $e$ ,  $\iota$  in the case of  $e_{\text{ini}} = 0.7$  with the

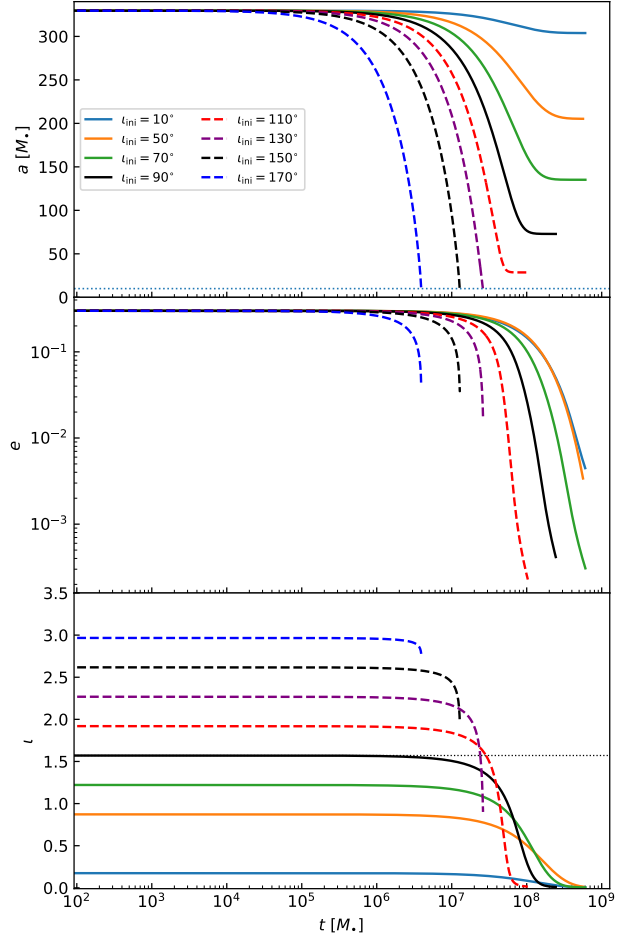


FIG. 5. Evolution of the semi-major axis  $a$ , eccentricity  $e$ , and orbital inclination angle  $\iota$  using the aero-drag force model with a constant damping coefficient  $\gamma_0 = 2 \times 10^{-6} M_\star^{-1}$ . The initial conditions are  $p_{\text{ini}} = 300 M_\star$ , and  $e_{\text{ini}} = 0.3$ . The prograde cases ( $\iota_{\text{ini}} < 90^\circ$ ) are shown with solid lines, while the retrograde cases ( $\iota_{\text{ini}} > 90^\circ$ ) are shown with dashed lines. The blue dotted horizontal line at  $a = 10 M_\star$  in the top panel marks the threshold below which the orbit is considered to have shrunk in this work. The black dotted horizontal line in the bottom panel marks  $\iota = \pi/2$ .

aero-drag force model is shown in the three panels of Fig. 6, with all other conditions identical to those for  $e_{\text{ini}} = 0.3$ . Overall, changing the initial eccentricity does not significantly affect the evolution of the orbital parameters.

## B. Orbital evolution of sBHs

In this subsection, we consider sBH-disk collisions, where the perturbing force is dominated by dynamical friction (10). The change rate of the eccentricity  $e$  as a function of the orbital inclination angle  $\iota$  is computed using the same method and initial conditions as in Fig. 3, except that the dynamical-friction model with  $\gamma_0 = 4 \times 10^{-13} M_\star^{-1}$  is adopted. The results are shown in Fig. 7. In contrast to the aero-drag force model, we find dynamical friction can increase the orbital eccentric-

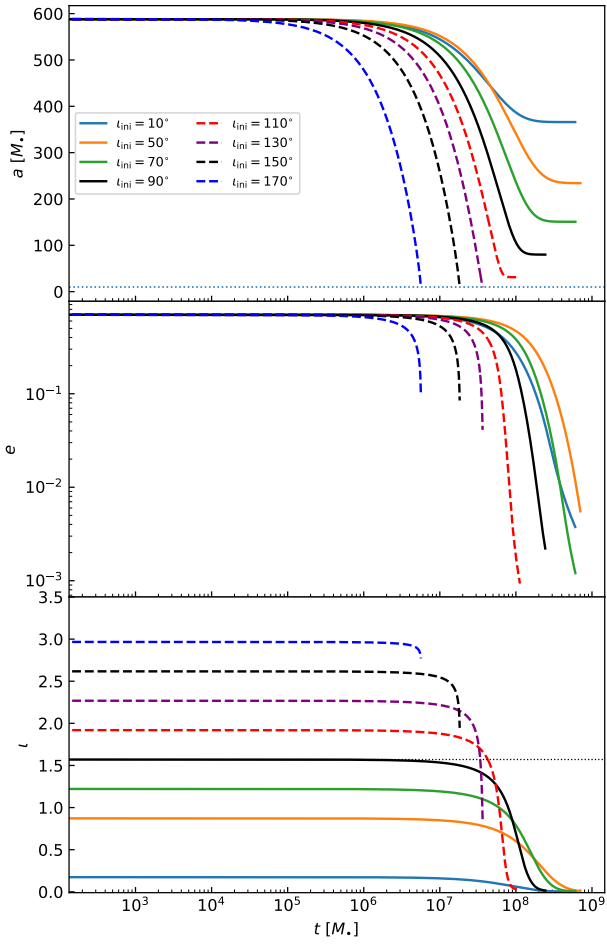


FIG. 6. Same as Fig. 5 except for  $e_{\text{ini}} = 0.7$ .

ity  $e$  if the orbiter is highly misaligned with  $\iota$  in the range of  $(\iota_{\text{crit}}, 180^\circ)$ , where  $\iota_{\text{crit}} \approx 60^\circ - 90^\circ$  for the parameter range considered in this work. Similar results were also found in previous studies [18, 19], which motivate some recent discussions on eccentric wet EMRIs. As we will show later in this section, EMRIs that are captured by disks are circularized due to the eccentricity damping when  $\iota < \iota_{\text{crit}}$ .

As discussed in Sec. III A, we also calculate two timescales  $\tau_a$  and  $\tau_t$  for the sBH orbit, as shown in Fig. 8, with the same set of initial conditions as in Fig. 7. The calculations also yield  $\langle da/d\tau \rangle < 0$  and  $\langle d\iota/d\tau \rangle < 0$  for all inclination angles, showing that the disk is aligning the orbiter. From Fig. 8, for the sBH-SMO cases, large initial orbital inclination angles result in  $\tau_a < \tau_t$ , consistent with the behavior found in the stellar-SMO cases, while  $\tau_t$  increases monotonically with  $\iota$ ,  $\tau_a$  initially increases with  $\iota$  because the larger relative velocity between the sBH and the disk material reduces the effect of the dynamical friction according to Eqs. (10) and (11), in contrast to the behavior under the aero-drag force model. It can also be found that  $\tau_a$  decreases as  $\iota \rightarrow \pi$ , which can be interpreted as the strengthened interaction resulting from the sBH orbit gradually becoming embedded in the disk plane.

To illustrate the evolution behavior and timescale hierarchy

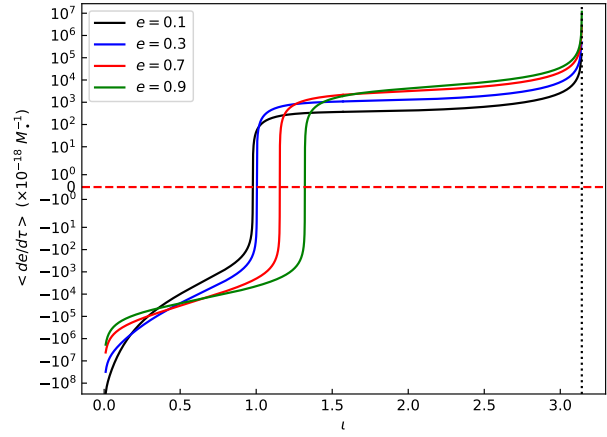


FIG. 7. The comparison of  $\langle \frac{de}{d\tau} \rangle$  variations with orbital inclination angle  $\iota$  for different  $e$ , with  $p_{\text{ini}} = 300 M_*$ , with the dynamical friction model for the sBH-SMO cases. The vertical black dotted line marks  $\iota = \pi$  ( $180^\circ$ ).

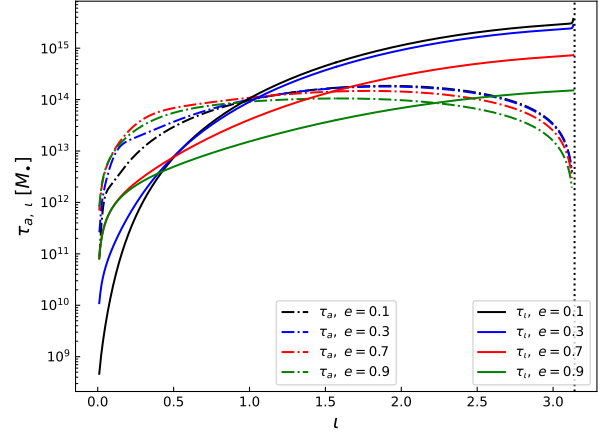


FIG. 8. The comparison of estimated shrink timescale with  $\tau_a = |a_{\text{ini}} / \langle \frac{da}{d\tau} \rangle_{\text{ini}}|$  (solid dotted line) and capture timescale with  $\tau_t = |\iota_{\text{ini}} / \langle \frac{d\iota}{d\tau} \rangle_{\text{ini}}|$  (solid line) with orbital inclination angle  $\iota$  for different  $e$ , fixing  $p_{\text{ini}} = 300 M_*$ , using the dynamical friction force model for the sBH-SMO cases. The vertical black dotted line marks  $\iota = \pi$  ( $180^\circ$ ).

discussed above, we now present representative numerical examples of the orbital evolution under the dynamical friction, computed within the adiabatic approximation. We consider orbits with an initial semi-latus rectum  $p_{\text{ini}} = 300 M_*$  and compute the evolution with different initial inclination angles, focusing on initial eccentricities of  $e_{\text{ini}} = 0.3, 0.7$ , under the dynamical-friction model with  $\gamma_0 = 4 \times 10^{-13} M_•^{-1}$ . The evolution of  $a$ ,  $e$ ,  $\iota$  for  $e_{\text{ini}} = 0.3$  under the dynamical friction model is shown in the three panels of Fig. 9. In this work, for dynamical friction model, the calculation is terminated once the orbit approaches the near-aligned configuration with the disk plane, as during the alignment process, the relative ve-

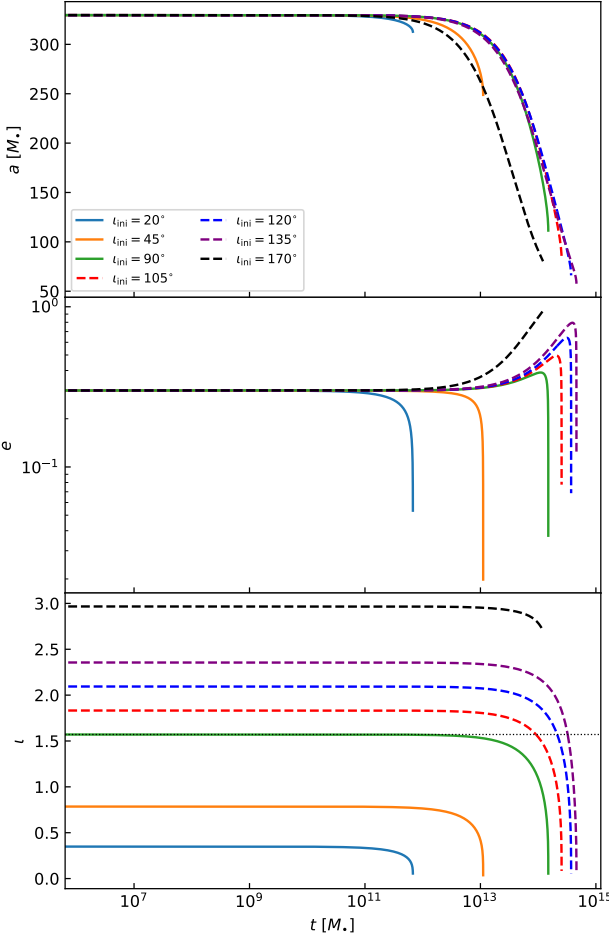


FIG. 9. Same as Fig. 5 except for using dynamical friction model with the constant part of damping coefficient  $\gamma_0 = 4 \times 10^{-13} M_\bullet^{-1}$ .

locity between the sBH and the disk gradually decreases, the change rate of the orbital parameters become sufficiently large and potentially invalidates the adiabatic approximation.

For cases with  $i_{\text{ini}} = 20^\circ - 135^\circ$ , near-complete alignment of the orbits occurs before significant orbital shrinkage. In contrast, for the higher inclination case with  $i_{\text{ini}} = 170^\circ$ , although the semi-major axis  $a$  is still several times of  $10 M_\bullet$ , the calculation is terminated before the condition  $p - 6 - 2e > 0$  is violated [48], which marks the transition from a stable to an unstable orbit and the inevitable infall of the sBH into the central SMBH.

As shown in the middle panel of Fig. 9, for all retrograde cases, the eccentricity is excited (see Fig. 7). For prograde cases, exemplified by  $i_{\text{ini}} = 90^\circ$ , the eccentricity is also initially excited. As  $i$  decreases, a transition occurs from  $\langle de/d\tau \rangle > 0$  to  $\langle de/d\tau \rangle < 0$ , and the eccentricity eventually declines. For smaller initial inclination angles, such as  $i_{\text{ini}} = 20^\circ, 45^\circ$ , the eccentricity decreases from the outset.

The evolution of  $a, e, i$  for  $e_{\text{ini}} = 0.7$  with the dynamical friction model is shown in the three panels of Fig. 10, with all other conditions identical to those for  $e_{\text{ini}} = 0.3$ . Overall, the evolution of the orbital parameters shows no significant

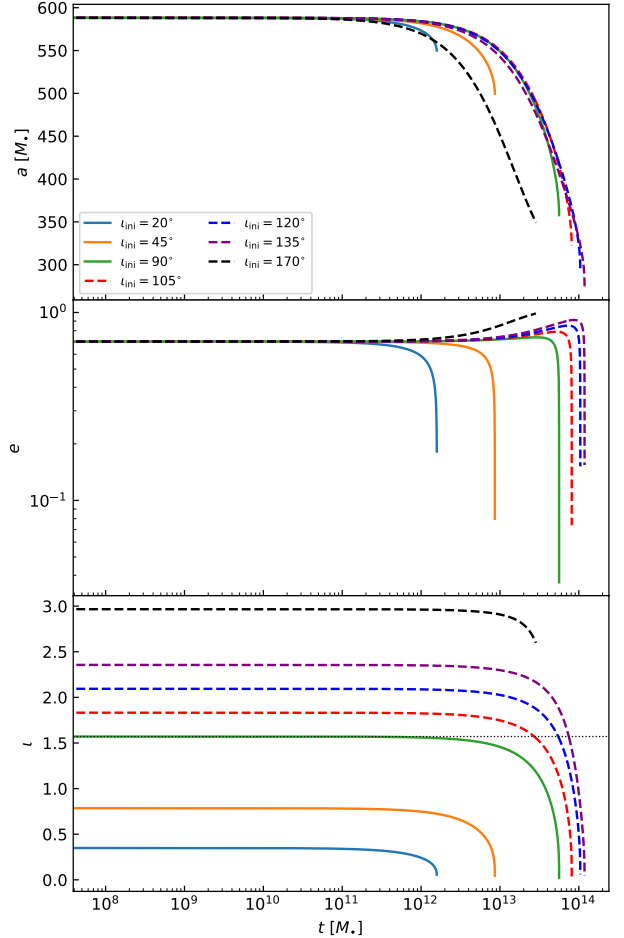


FIG. 10. Same as Fig. 9 except for  $e_{\text{ini}} = 0.7$ .

differences compared to the  $e_{\text{ini}} = 0.3$  case.

### C. Capture timescales of AGN disks

As shown in the preceding subsections, collisions with the disk drive a secular decrease in the orbital inclination angle  $i$ , which may ultimately lead to the SMO being captured by the disk. In this subsection, we estimate characteristic timescales for SMOs to be captured by the disk in EMRI systems over a wide range of orbital scales.

We first analyze the dependence of the capture timescale  $t_{\text{cap}}$  on relevant quantities of the EMRI+disk system. For clarity, starting from the aero-drag force model in Eq. (9), we note that the coefficients  $C_{z1}(\theta), C_{z1}(\phi)$  given in Appendix B scale as  $p^{3/2}$ , while the  $\theta, \phi$  acceleration components in Appendix A scale as

$$\gamma_0 |v_{\text{rel}}| p^{-3/2} \sim \gamma_0 p^{-1/2} p^{-3/2} \sim \gamma_0 p^{-2}, \quad (31)$$

where  $|v_{\text{rel}}|$  can be approximated using the Keplerian relation that  $|v_{\text{rel}}| \sim p^{-1/2}$ . Combining this with the crossing time of the SMO through the disk with the height  $H_{\text{disk}}$ , which can be approximated using the Keplerian estimate  $t_{\text{cross}} \sim$

$H_{\text{disk}} v_{\text{SMO}}^{-1} \sim H_{\text{disk}} p^{1/2}$ , and using  $z_1 = \sin \iota$ , we find that the change in  $\iota$  produced by each SMO–disk collision scales as

$$\Delta \iota \sim \Delta z_1 \sim p^{\frac{3}{2}} \cdot \gamma_0 p^{-2} \cdot H_{\text{disk}} p^{\frac{1}{2}} \sim \Sigma_g R_{\star}^2 m_{\star}^{-1}. \quad (32)$$

Thus, the total number of collisions required for a given inclination angle  $\iota$  to decrease from its initial value to nearly zero scales as

$$N_{\text{cap}} \sim \Sigma_g^{-1} R_{\star}^{-2} m_{\star}. \quad (33)$$

Since the orbital period of the SMO scales as  $T_{\text{orb}} \sim p^{3/2}$ , the capture timescale follows

$$t_{\text{cap}} \sim N_{\text{cap}} T_{\text{orb}} \sim \Sigma_g^{-1} R_{\star}^{-2} m_{\star} p^{3/2}. \quad (34)$$

The power law relations  $t_{\text{cap}} \sim p^n$  for the dynamical friction model can be derived in a similar manner. In both cases, the dependence of the damping coefficient on the relative velocity  $|v_{\text{rel}}|$  should be taken into account. The resulting power law relations for both interaction models are summarized in Table. I.

As a numerical example, shown in Fig. 11, we examine the dependence of the capture timescale  $t_{\text{cap}}$  on the initial semi-latus rectum  $p_{\text{ini}}$  using the aero-drag force model with the damping coefficient  $\gamma_0 = 2 \times 10^{-6} M_{\bullet}^{-1}$ .  $p_{\text{ini}}$  is sampled over in the range  $(300, 2000) M_{\bullet}$ , for two initial inclination angles,  $\iota_{\text{ini}} = 45^\circ$  and  $90^\circ$ , while the initial eccentricity fixed at  $e_{\text{ini}} = 0.3$ . For clarity, we define the capture timescale  $t_{\text{cap}}$  as the coordinate time at which the orbital inclination decreases from its initial value  $\iota_{\text{ini}}$  to a small threshold  $\iota_{\text{crit}} = 1.5 \times 10^{-2}$ . The numerical results are well consistent with the expected scaling  $t_{\text{cap}} \sim p^{3/2}$ .

TABLE I. Power scaling relations between  $t_{\text{cap}}$  and  $p$  and other parameters

Model	$f^{\mu}$	$N_{\text{cap}}$	$t_{\text{cap}}$
Aero-drag	$\sim \gamma_0  \mathbf{v}_{\text{vel}}  u_{\text{vel}}^{\mu}$	$\sim \Sigma_g^{-1} R_{\star}^{-2} m_{\star} p^0$	$\sim \Sigma_g^{-1} R_{\star}^{-2} m_{\star} p^{\frac{3}{2}}$
Dynamical friction	$\sim \gamma_0  \mathbf{v}_{\text{vel}} ^{-3} u_{\text{vel}}^{\mu}$	$\sim \Sigma_g^{-1} m_{\bullet}^{-1} p^{-2}$	$\sim \Sigma_g^{-1} m_{\bullet}^{-1} p^{-\frac{1}{2}}$

To assess whether misaligned EMRIs can be captured by the AGN disk within a certain timescale, we estimate the disk-capture timescale using scaling relations in Table. I. The capture timescale is evaluated with  $p_{\text{ini}} = 300 M_{\bullet}$ , and  $e_{\text{ini}} = 0.3$ , in combination with the Sirk & Goodman (SG) disk model [49]. For simplicity, we restrict our analysis to cases in which orbital alignment occurs prior to significant orbital shrinkage. We adopt the same conventions as in Ref. [19] for the SMO mass, taking  $m_{\star} = m_{\bullet} = 30 M_{\odot}$ , and for stellar SMOs, the stellar radius is set to  $R_{\star} = R_{\odot} (m_{\star}/M_{\odot})^{\frac{3}{4}}$ . The disk surface-density and scale-height profiles are obtained using the Sirk module in the pagn package [50] (see Fig. 12).

For the aero-drag force model, the results presented in Figs. 5 and 6 show that the capture timescale in prograde cases is longer than in retrograde cases. The estimates are carried out for initial inclination angles  $\iota_{\text{ini}} = 10^\circ, 30^\circ, 50^\circ, 70^\circ, 90^\circ$  and for SMBH masses of  $M_{\bullet} = 10^6 M_{\odot}, 10^8 M_{\odot}$ , with the

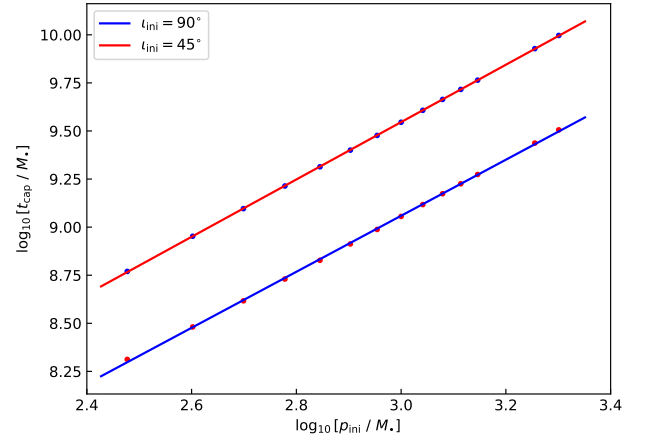


FIG. 11. Dependence of the capture timescale on the initial semi-latus rectum  $p_{\text{ini}}$  over the range  $300 M_{\bullet}$  to  $2000 M_{\bullet}$ , computed using the aero-drag force model.

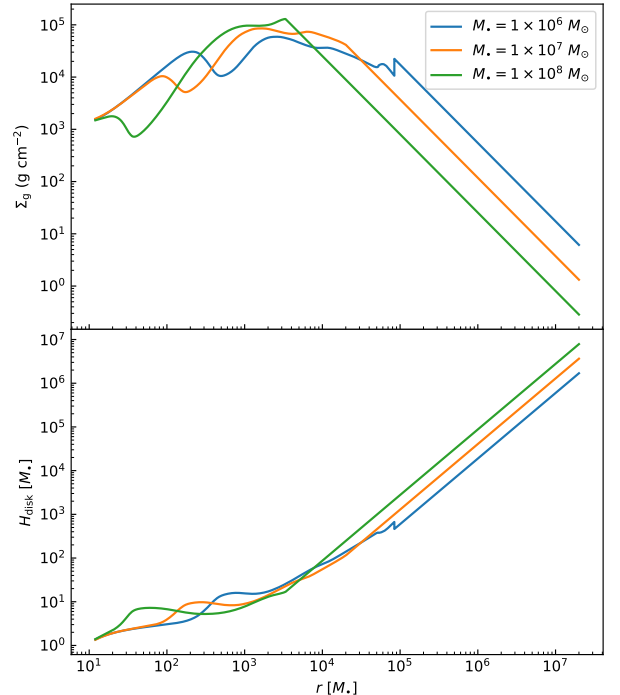


FIG. 12. The surface density  $\Sigma_g$  and disk height  $H_{\text{disk}}$  distribution with the radial distance  $r$  from the central SMBH with different masses, for SG disk model, with the Eddington ratio  $l_e = 0.5$ , viscosity parameter  $\alpha = 0.1$ , hydrogen abundance  $X = 0.7$ , and  $\alpha$ –disk case with  $b = 0$ .

results shown in two panels of Fig. 13, respectively. For prograde cases under the aero-drag force model, the capture timescale exhibits only a weak dependence on the initial orbital inclination angle, as can be seen in Figs. 5 and 6. This behavior can be interpreted as follows. Larger orbital inclinations lead to higher relative velocities, which in turn produce larger inclination-change rates. As a result, once the inclination exceeds a certain threshold, the alignment timescale decreases.

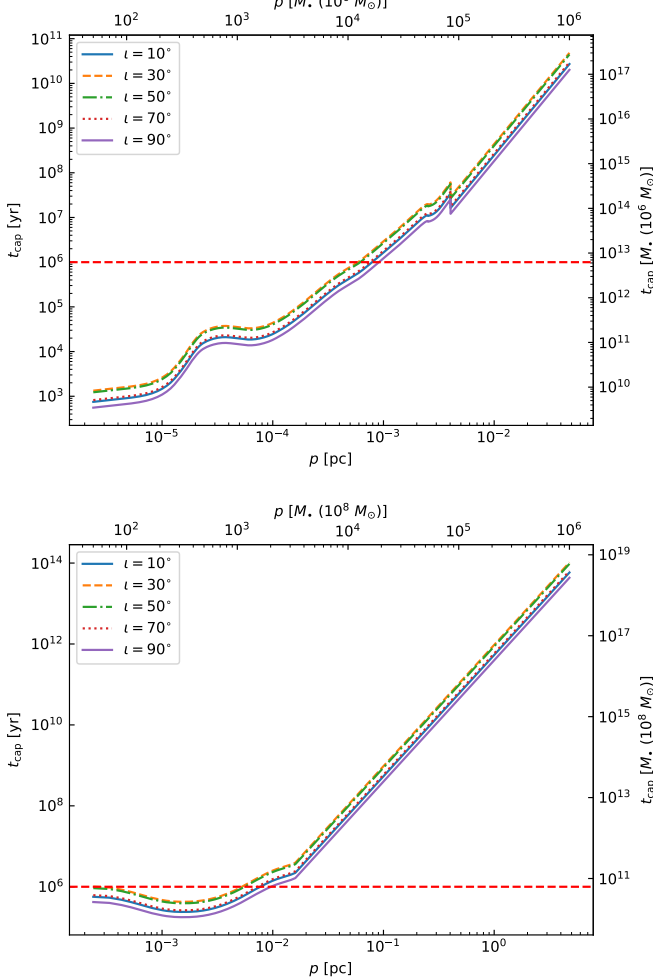


FIG. 13. Capture timescales estimated using the aero-drag force model for initial inclination angles  $i_{\text{ini}} = 10^\circ, 30^\circ, 50^\circ, 70^\circ, 90^\circ$ . The horizontal red dashed line indicates  $t = 10^6$  yr. The top and bottom panels correspond to SMBH masses of  $M_\bullet = 10^6 M_\odot$  and  $10^8 M_\odot$ , respectively.

For the dynamical friction model, the timescale estimates are evaluated for SMBH masses of  $M_\bullet = 10^6 M_\odot, 10^7 M_\odot$  and  $10^8 M_\odot$ , as shown in three panels of Fig. 14, respectively. In the dynamical friction model, the capture timescale increases significantly with orbital inclination, since larger relative velocities lead to smaller inclination-change rates.

For both models, the capture timescale is compared with a critical timescale of  $10^6$  yr (1 Myr). For the aero-drag force

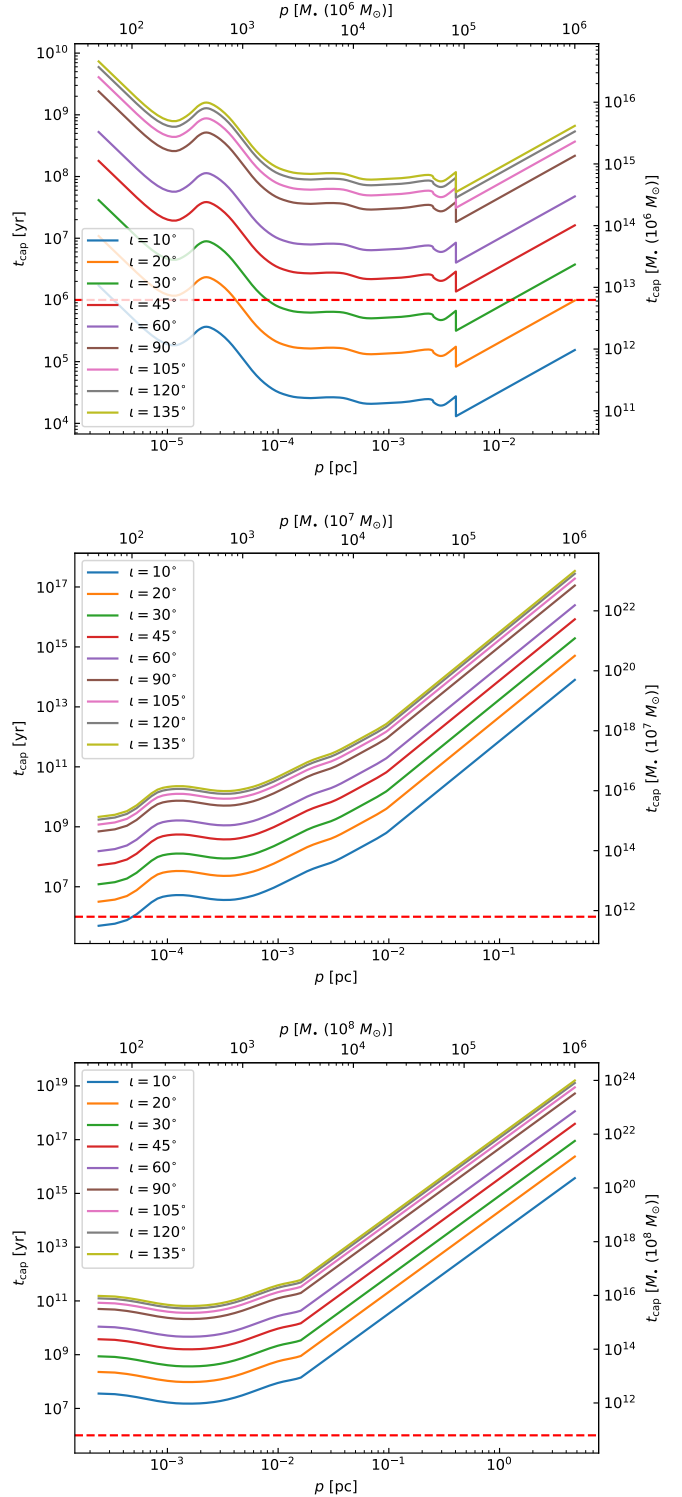


FIG. 14. Capture timescales estimated using the dynamical friction model for initial inclination angles  $i_{\text{ini}} = 10^\circ, 20^\circ, 30^\circ, 45^\circ, 60^\circ, 90^\circ, 105^\circ, 120^\circ, 135^\circ$ . The horizontal red dashed line indicates  $t = 10^6$  yr. The top, middle and bottom panels correspond to SMBH masses of  $M_\bullet = 10^6 M_\odot, 10^7 M_\odot$  and  $10^8 M_\odot$ , respectively.

model, SMOs at distances of order  $10^{-3}$  pc can be captured within 1 Myr for  $M_\bullet = 10^6 M_\odot$ , whereas this distance increases to about  $10^{-2}$  pc for  $M_\bullet = 10^8 M_\odot$ . For the dynamical friction model, the range of orbital inclination angles for which SMOs can be captured within 1 Myr decreases noticeably with increasing SMBH mass, primarily due to the disk surface-density profile and the scaling between the SMBH mass  $M_\bullet$  and physical time. The distribution profiles of the estimated capture timescales for  $M_\bullet = 10^6 M_\odot$  differ from those in the other two cases, primarily due to differences in the disk surface density profiles (see Fig. 12).

#### D. Comparison with previous studies

In previous studies [1, 18–24] of star–disk collisions in EMRIs, the orbital evolution of the SMO is typically modeled within a Newtonian framework. The secular changes are commonly estimated by summing the contributions from the two disk crossings within one orbital period and dividing by the orbital period. In this section, we compare the evolution of the orbital parameters  $a$ ,  $e$  and  $\iota$  for the stellar-SMO and sBH-SMO cases, obtained under the adiabatic approximation in Schwarzschild spacetime and shown in Figs. 5–10, with those reported in previous studies.

Our calculations broadly agree with the results of [19]. Consistent with [18] and [19], we find that collisions with the disk always tends to align the SMO no matter what the initial orbital inclination  $\iota_{\text{ini}}$  is. An opposite trend was claimed in [22] for sBHs with large initial inclination angles. The authors cautioned that this peculiar behavior might reflect missing physics, such as the inconsistent assumption of circular orbits and the neglect of disk back reaction on the orbiting object. Consistent with [18] and [19], we find star-disk collisions always circularize the star orbit, while sBH-disk collisions excite the orbital eccentricity when the orbital inclination  $\iota$  is large. But the temporary orbital eccentricity excitation does not lead to formation of eccentric wet EMRIs because the orbital eccentricity is largely damped when the inclination decreases and approaches zeros when the orbiter is captured by the disk (Figs. 9, 10).

In [23], the authors found that the orbital eccentricity of embedded retrograde EMRIs can be efficiently excited to near unity by dynamical friction. This behavior is qualitatively consistent with the eccentricity growth observed in our high-inclination sBH cases, particularly for  $\iota_{\text{ini}} = 170^\circ$  (see Figs. 9, 10). The finding has been used for argument of formation of eccentric wet EMRIs in AGN disks. In fact, as we have found in this work by tracking full orbital evolution of EMRIs, AGN disks always tend to align EMRIs that are initially misaligned, and the captured EMRIs are effectively circularized though the orbital eccentricity may be temporarily excited during the capture process (Figs. 9, 10). As a result, there is little parameter space for forming eccentric wet retrograde EMRIs.

In addition to these qualitative agreement, our calculations also show quantitative agreement with [19] e.g., in the capture timescale of sBHs by AGN disks. For the sBHs, we adopt a constant damping coefficient  $\gamma_0 = 4 \times 10^{-13} M_\bullet^{-1}$ ,

together with the disc scale height  $H_{\text{disk}} = 1.5 M_\bullet$ . According to Eq. (11), the remaining factors entering the damping coefficient can be combined into the dimensionless normalization  $(\Sigma_g/10^5 \text{ g} \cdot \text{cm}^{-2}) \cdot (m_\bullet/M_\odot) \approx 86.58$ . In Ref. [19], sBHs were modeled with an initial semi-major axis  $a_{\text{ini}} = 10^{-3}$  pc and eccentricity  $e_{\text{ini}} = 0.7$ , which correspond to an initial semi-latus rectum  $p_{\text{ini}} \sim 10^2 M_\bullet$ , for a central SMBH of  $M_\bullet = 10^8 M_\odot$ . Adopting the surface density profile implied by the  $\alpha$ -disk model shown in their work, and using the scaling relations listed in Table I, together with the numerical results obtained in this work (see Fig. 10), we find that the resulting capture timescales are consistent at the order-of-magnitude level. We note that the capture timescales reported in Ref. [19] are systematically shorter than those obtained here, likely because their disc model implies an increasing surface density as the orbit shrinks, whereas a constant surface density assumption is adopted in this work; nevertheless, the overall scaling remains consistent.

## IV. CONCLUSION

In this work, we study the orbital evolution of EMRI driven by interactions with accretion disks in a relativistic framework. We derive the secular evolution of the key orbital parameters, the semi-major axis  $a$ , eccentricity  $e$ , and orbital inclination angle  $\iota$ , by adopting the double-phase average formulation (28), which is suitable for adiabatic evolution over the proper time  $\tau$ . Building on this relativistic framework, we develop a theoretical model for SMO–disk collisions under the thin-disk assumption and analyze the resulting orbital evolution under two representative interaction mechanisms: aero-drag and dynamical friction forces, which capture the essential features of star and sBH crossings.

Under both the aero-drag and dynamical friction forces,  $a$  and  $\iota$  decrease monotonically in both prograde and retrograde configurations, reflecting orbital-energy dissipation and the tendency toward angular-momentum alignment between the orbit and the disk. The eccentricity  $e$  decreases monotonically under aero-drag force, leading to a steadily circularizing orbit, whereas under dynamical friction it can be excited at sufficiently large inclinations in some prograde cases and throughout the retrograde cases. In addition, based on the numerical results, we find that the orbit becomes nearly circularized as the SMO is captured by the disk or as its orbit shrinks.

Based on the SG disk model and the scaling relations derived for different interaction mechanisms, together with the alignment times inferred from the representative cases computed in this work, we estimate the capture timescales for wider orbits around SMBHs of various masses and assess the feasibility of capturing SMOs within the timespan of 1 Myr. We find only a small fraction of sBHs that are initially close to the SMBH and close to the disk can be captured by the disk within typical disk lifetime of active galactic nuclei. Therefore, two-body scatterings between sBHs and stars in the nuclear stellar cluster play an essential role in randomly kicking EMRIs towards the disk and boosting the capture rate [35].

We have also derived a power-law dependence of the cap-

ture timescale on the initial semi-latus rectum  $p$ . Specifically, we find  $t_{\text{cap}} \sim p^{3/2}$  for the aero-drag force model and  $t_{\text{cap}} \sim p^{-1/2}$  for the dynamical friction model. These scalings are obtained based on the evolution equation of the orbital inclination angle  $\iota$  and the disk-crossing process. We then compare the orbital evolution and the capture timescales obtained in this work with those reported in several previous studies. We find that the orbital evolution behavior identified here is broadly consistent with most of the existing literature. Moreover, by applying the scaling relations listed in Table I together with more realistic disk surface density models, the estimated capture timescales can be consistent with previous results at the order-of-magnitude level.

### Appendix A: Basic form of acceleration components

With the basic acceleration form of Eq. (3), with  $u_{\text{ZAMO}}^\mu$  substituted with  $u_{\text{disk}}^\mu$ , the  $r$ ,  $\theta$ ,  $\phi$  components of the acceleration can be expressed as

$$\begin{aligned} f^r(\psi, \chi) &= -\gamma_{\text{gas}}(\psi, \chi)u^r \\ &= -\gamma_{\text{gas}}(\psi, \chi)\sqrt{\frac{p-6-2e\cos(\psi-\psi_0)}{p(p-3-e^2)}}e\sin(\psi-\psi_0), \end{aligned} \quad (\text{A1})$$

$$\begin{aligned} f^\theta(\psi, \chi) &= -\gamma_{\text{gas}}(\psi, \chi)u^\theta \\ &= -\gamma_{\text{gas}}(\psi, \chi)\frac{[1+e\cos(\psi-\psi_0)]^2}{p\sqrt{p-3-e^2}}\cdot\frac{z_1\sin(\chi-\chi_0)}{\sqrt{1-z_1^2\cos^2(\chi-\chi_0)}}, \end{aligned} \quad (\text{A2})$$

$$\begin{aligned} f^\phi(\psi, \chi) &= -\gamma_{\text{gas}}(\psi, \chi)\left(u^\phi+\frac{u_{\text{gas}}^\phi}{u_t^{\text{gas}}u^t+u_\phi^{\text{gas}}u^\phi}\right) \\ &= -\gamma_{\text{gas}}(\psi, \chi)\left\{\frac{[1+e\cos(\psi-\psi_0)]^2}{p\sqrt{p-3-e^2}}\cdot\frac{\sqrt{1-z_1^2}}{1-z_1^2\cos^2(\chi-\chi_0)}\right. \\ &\quad \left.+\frac{\sqrt{p-3-e^2}}{p\sqrt{1-z_1^2}-\frac{p\sqrt{(p-2)^2-4e^2}}{[1+e\cos(\psi-\psi_0)]^{\frac{3}{2}}}}\right\}. \end{aligned} \quad (\text{A3})$$

### Appendix B: Coefficients $C_{r,\theta,\phi}^{(I_0)}$

The detailed expressions of the coefficients for  $p$ ,  $e$ , and  $z_1$  in Eq. (26) are

$$\begin{aligned} C_r^{(p)} &= -\frac{2(p-3-e^2)}{(p-6)^2-4e^2}\sqrt{\frac{e^2p^3[p-2e\cos(\psi-\psi_0)-6]}{p-3-e^2}} \\ &\quad \cdot\sin(\psi-\psi_0), \end{aligned} \quad (\text{B1})$$

$$\begin{aligned} C_\theta^{(p)} &= \frac{2p^2z_1\sin(\chi-\chi_0)\sqrt{p-3-e^2}}{[(p-6)^2-4e^2]\sqrt{1-z_1^2\cos^2(\chi-\chi_0)}[1+e\cos(\psi-\psi_0)]^2} \\ &\quad \cdot[18-9p+p^2-2e(-3+p)\cos(\psi-\psi_0)-e^2(-6+p) \\ &\quad \cdot\cos^2(\psi-\psi_0)+2e^3\cos^3(\psi-\psi_0)], \end{aligned} \quad (\text{B2})$$

$$\begin{aligned} C_\phi^{(p)} &= \frac{2p^2\sqrt{(p-3-e^2)(1-z_1^2)}}{[(p-6)^2-4e^2][1+e\cos(\psi-\psi_0)]^2} \\ &\quad \cdot[18-9p+p^2-2e(-3+p)\cos(\psi-\psi_0)-e^2(-6+p) \\ &\quad \cdot\cos^2(\psi-\psi_0)+2e^3\cos^3(\psi-\psi_0)], \end{aligned} \quad (\text{B3})$$

$$\begin{aligned} C_r^{(e)} &= \frac{(p-6-2e^2)\sin(\psi-\psi_0)}{(p-6)^2-4e^2} \\ &\quad \cdot\sqrt{p(p-3-e^2)[p-6-2e\cos(\psi-\psi_0)]}, \end{aligned} \quad (\text{B4})$$

$$\begin{aligned} C_\theta^{(e)} &= \frac{pz_1\sin(\chi-\chi_0)\sqrt{p-3-e^2}}{[(p-6)^2-4e^2]\sqrt{1-z_1^2\cos^2(\chi-\chi_0)}[1+e\cos(\psi-\psi_0)]^2} \\ &\quad \cdot[e(12+4e^2-10p+p^2)-2(6+2e^2-p)(-3+p) \\ &\quad \cdot\cos(\psi-\psi_0)-e(6+2e^2-p)(-6+p)\cos^2(\psi-\psi_0) \\ &\quad +2e^2(6+2e^2-p)\cos^3(\psi-\psi_0)], \end{aligned} \quad (\text{B5})$$

$$\begin{aligned} C_\phi^{(e)} &= \frac{p\sqrt{(p-3-e^2)(1-z_1^2)}}{[(p-6)^2-4e^2][1+e\cos(\psi-\psi_0)]^2} \\ &\quad \cdot[e(12+4e^2-10p+p^2)-2(6+2e^2-p)(-3+p) \\ &\quad \cdot\cos(\psi-\psi_0)-e(6+2e^2-p)(-6+p)\cos^2(\psi-\psi_0) \\ &\quad +2e^2(6+2e^2-p)\cos^3(\psi-\psi_0)], \end{aligned} \quad (\text{B6})$$

$$C_r^{(z_1)} = 0, \quad (\text{B7})$$

$$C_\theta^{(z_1)} = \frac{p(1-z_1^2)\sin(\chi-\chi_0)\sqrt{p-3-e^2}}{\sqrt{1-z_1^2\cos^2(\chi-\chi_0)}[1+e\cos(\psi-\psi_0)]^2}, \quad (\text{B8})$$

$$C_\phi^{(z_1)} = -\frac{pz_1\sin^2(\chi-\chi_0)\sqrt{(p-3-e^2)(1-z_1^2)}}{[1+e\cos(\psi-\psi_0)]^2}. \quad (\text{B9})$$

For  $\psi_0$  and  $\chi_0$ , with

$$\begin{aligned} \frac{d\psi_r}{d\tau} &= \frac{d\psi}{d\tau} - \frac{d\psi_0}{d\tau} = \frac{d\psi_r}{d\tau} \Big|_{\text{geodesic}} - \frac{d\psi_0}{d\tau} \\ &= \frac{1}{(\partial r/\partial\psi_r)}\left(\frac{dr}{d\tau} - \frac{1}{(\partial r/\partial\psi_r)}\frac{\partial r}{\partial p}\frac{dp}{d\tau} - \frac{\partial r}{\partial e}\frac{de}{d\tau}\right), \end{aligned} \quad (\text{B10})$$

and

$$\begin{aligned} \frac{d\psi_\theta}{d\tau} &= \frac{d\chi}{d\tau} - \frac{d\chi_0}{d\tau} = \frac{d\psi_\theta}{d\tau} \Big|_{\text{geodesic}} - \frac{d\chi_0}{d\tau} \\ &= \frac{1}{(\partial\theta/\partial\psi_\theta)}\left(\frac{d\theta}{d\tau} - \frac{\partial\theta}{\partial z_1}\frac{dz_1}{d\tau}\right), \end{aligned} \quad (\text{B11})$$

then

$$C_r^{(\psi_0)} = -\frac{(p-6)\cos(\psi-\psi_0) + 2e}{e[(p-6)^2 - 4e^2]} \cdot \sqrt{p(p-3-e^2)[p-6-2e\cos(\psi-\psi_0)]}, \quad (\text{B12})$$

$$C_\theta^{(\psi_0)} = -\frac{pz_1\sin(\chi-\chi_0)\sin(\psi-\psi_0)\sqrt{p-3-e^2}}{e[(p-6)^2-4e^2]\sqrt{1-z_1^2\cos^2(\chi-\chi_0)[1+e\cos(\psi-\psi_0)]^2}} \cdot \{e[4e^2-(p-6)^2]\cos(\psi-\psi_0) + (-6+p)(6+e^2-2p+e^2\cos[2(\psi-\psi_0)])\}, \quad (\text{B13})$$

$$C_\phi^{(\psi_0)} = -\frac{p\sqrt{(p-3-e^2)(1-z_1^2)}\sin(\psi-\psi_0)}{e[(p-6)^2-4e^2][1+e\cos(\psi-\psi_0)]} \cdot \{e[4e^2-(p-6)^2]\cos(\psi-\psi_0) + (-6+p)(6+e^2-2p+e^2\cos[2(\psi-\psi_0)])\}, \quad (\text{B14})$$

$$C_r^{(\chi_0)} = 0, \quad (\text{B15})$$

$$C_\theta^{(\chi_0)} = -\frac{p\sqrt{p-3-e^2}(1-z_1^2)\cos(\chi-\chi_0)}{z_1\sqrt{1-z_1^2\cos^2(\chi-\chi_0)[1+e\cos(\psi-\psi_0)]^2}}, \quad (\text{B16})$$

$$C_\phi^{(\chi_0)} = \frac{p\sqrt{(p-3-e^2)(1-z_1^2)}\sin[2(\chi-\chi_0)]}{2[1+e\cos(\psi-\psi_0)]^2}. \quad (\text{B17})$$

### Appendix C: Adiabatic approximation form in this work

In this work, by explicitly accounting for  $\psi_0$  and  $\chi_0$ , we adopt an equivalent form of Eq. (28), in which the phases  $\psi$  and  $\chi$  are integrated from 0 to  $2\pi$ , as

$$\langle f \rangle_{I_0} = \frac{\int_0^{2\pi} d\chi \int_0^{2\pi} d\psi \frac{1}{\omega_r(\psi_r, \mathbf{I})} f(\psi_r, \psi_\theta, \mathbf{I})}{2\pi \int_0^{2\pi} d\psi \frac{1}{\omega_r(\psi_r, \mathbf{I})}}, \quad (\text{C1})$$

with  $\psi_r = \psi - \psi_0$ ,  $\psi_\theta = \chi - \chi_0$ ,  $\mathbf{I} = \{p, e, z_1\}$  and  $I_0 = \{p, e, z_1, \psi_0, \chi_0\}$ .

---

[1] C. E. O'Connor and D. Lai, *Monthly Notices of the Royal Astronomical Society* **498**, 4005 (2020).

[2] W. Kley and R. Nelson, *Annual Review of Astronomy and Astrophysics* **50**, 211 (2012).

[3] Kuwahara, Ayumu, Kurokawa, Hiroyuki, and Ida, Shigeru, *A&A* **623**, A179 (2019).

[4] Y. Yang, I. Bartos, Z. Haiman, B. Kocsis, Z. Márka, N. C. Stone, and S. Márka, *The Astrophysical Journal* **876**, 122 (2019).

[5] P. Peng, A. Franchini, M. Bonetti, A. Sesana, and X. Chen, *The Astrophysical Journal* **989**, 122 (2025).

[6] B. McKernan, K. E. S. Ford, W. Lyra, H. B. Perets, L. M. Winter, and T. Yaqoob, *Monthly Notices of the Royal Astronomical Society: Letters* **417**, L103 (2011).

[7] Y. Levin, *Monthly Notices of the Royal Astronomical Society* **374**, 515 (2006).

[8] N. C. Stone, B. D. Metzger, and Z. Haiman, *Monthly Notices of the Royal Astronomical Society* **464**, 946 (2016).

[9] H. Tagawa, Z. Haiman, and B. Kocsis, *The Astrophysical Journal* **898**, 25 (2020).

[10] J. Xian, F. Zhang, L. Dou, J. He, and X. Shu, *The Astrophysical Journal Letters* **921**, L32 (2021).

[11] I. Linial and B. D. Metzger, *The Astrophysical Journal* **957**, 34 (2023).

[12] Franchini, Alessia, Bonetti, Matteo, Lupi, Alessandro, Miniutti, Giovanni, Bortolas, Elisa, Giustini, Margherita, Dotti, Massimo, Sesana, Alberto, Arcodia, Riccardo, and Ryu, Taeho, *A&A* **675**, A100 (2023).

[13] H. Tagawa and Z. Haiman, *Monthly Notices of the Royal Astronomical Society* **526**, 69 (2023).

[14] C. Zhou, L. Huang, K. Guo, Y.-P. Li, and Z. Pan, *Phys. Rev. D* **109**, 103031 (2024).

[15] C. Zhou, B. Zhong, Y. Zeng, L. Huang, and Z. Pan, *Phys. Rev. D* **110**, 083019 (2024).

[16] C. Zhou, Y. Zeng, and Z. Pan, *The Astrophysical Journal* **985**, 242 (2025).

[17] Lescaudron, Sandrine, Dubois, Yohan, Beckmann, Ricarda S., and Volonteri, Marta, *A&A* **674**, A217 (2023).

[18] T. F. M. Spieksma and E. Cannizzaro, (2025), arXiv:2504.08033 [astro-ph.GA].

[19] Y. Wang, Z. Zhu, and D. N. C. Lin, *Monthly Notices of the Royal Astronomical Society* **528**, 4958 (2024).

[20] C. Rowan, H. Whitehead, G. Fabj, P. Kirkeberg, M. E. Pessah, and B. Kocsis, *Monthly Notices of the Royal Astronomical Society* **543**, 132–145 (2025).

[21] G. Fabj, S. S. Nasim, F. Caban, K. E. S. Ford, B. McKernan, and J. M. Bellovary, *Monthly Notices of the Royal Astronomical Society* **499**, 2608 (2020).

[22] S. S. Nasim, G. Fabj, F. Caban, A. Secunda, K. E. S. Ford, B. McKernan, J. M. Bellovary, N. W. C. Leigh, and W. Lyra, *Monthly Notices of the Royal Astronomical Society* **522**, 5393 (2023).

[23] A. Secunda, B. Hernandez, J. Goodman, N. W. C. Leigh, B. McKernan, K. E. S. Ford, and J. I. Adorno, *The Astrophysical Journal Letters* **908**, L27 (2021).

[24] M. MacLeod and D. N. C. Lin, (2019), 10.3847/1538-4357/ab64db, arXiv:1909.09645 [astro-ph.SR].

[25] J. Baker *et al.*, (2019), arXiv:1907.06482 [astro-ph.IM].

[26] J. Mei, Y.-Z. Bai, J. Bao, E. Barausse, L. Cai, E. Canuto, B. Cao, W.-M. Chen, Y. Chen, Y.-W. Ding, H.-Z. Duan, H. Fan, W.-F. Feng, H. Fu, Q. Gao, T. Gao, Y. Gong, X. Gou, C.-Z. Gu, D.-F. Gu, Z.-Q. He, M. Hendry, W. Hong, X.-C. Hu, Y.-M. Hu, Y. Hu, S.-J. Huang, X.-Q. Huang, Q. Jiang, Y.-Z. Jiang, Y. Jiang, Z. Jiang, H.-M. Jin, V. Korol, H.-Y. Li, M. Li, M. Li, P. Li, R. Li, Y. Li, Z. Li, Z.-X. Li, Y.-R. Liang, Z.-C. Liang, F.-J. Liao, Q. Liu, S. Liu, Y.-C. Liu, L. Liu, P.-B. Liu, X. Liu, Y. Liu, X.-F. Lu, Y. Lu, Z.-H. Lu, Y. Luo, Z.-C. Luo,

V. Milyukov, M. Ming, X. Pi, C. Qin, S.-B. Qu, A. Sesana, C. Shao, C. Shi, W. Su, D.-Y. Tan, Y. Tan, Z. Tan, L.-C. Tu, B. Wang, C.-R. Wang, F. Wang, G.-F. Wang, H. Wang, J. Wang, L. Wang, P. Wang, X. Wang, Y. Wang, Y.-F. Wang, R. Wei, S.-C. Wu, C.-Y. Xiao, X.-S. Xu, C. Xue, F.-C. Yang, L. Yang, M.-L. Yang, S.-Q. Yang, B. Ye, H.-C. Yeh, S. Yu, D. Zhai, C. Zhang, H. Zhang, J.-d. Zhang, J. Zhang, L. Zhang, X. Zhang, X. Zhang, H. Zhou, M.-Y. Zhou, Z.-B. Zhou, D.-D. Zhu, T.-G. Zi, and J. Luo, *Progress of Theoretical and Experimental Physics* **2021**, 05A107 (2020).

[27] Z. Luo, Y. Wang, Y. Wu, W. Hu, and G. Jin, *Progress of Theoretical and Experimental Physics* **2021**, 05A108 (2020).

[28] P. Amaro-Seoane, *Living Rev. Relativity* **21**, 4 (2018).

[29] L. Barack and A. Pound, *Rept. Prog. Phys.* **82**, 016904 (2019).

[30] J. R. Gair, M. Vallisneri, S. L. Larson, and J. G. Baker, *Living Rev. Rel.* **16**, 7 (2013).

[31] G. Sigl, J. Schnittman, and A. Buonanno, *Phys. Rev. D* **75**, 024034 (2007).

[32] Z. Pan and H. Yang, *Phys. Rev. D* **103**, 103018 (2021).

[33] Z. Pan, Z. Lyu, and H. Yang, *Phys. Rev. D* **104**, 063007 (2021).

[34] Z. Pan and H. Yang, *The Astrophysical Journal* **923**, 173 (2021).

[35] Z. Pan, Z. Lyu, and H. Yang, *Phys. Rev. D* **105**, 083005 (2022).

[36] A. Derdzinski and L. Mayer, *Monthly Notices of the Royal Astronomical Society* **521**, 4522 (2023).

[37] B. Kocsis, N. Yunes, and A. Loeb, *Phys. Rev. D* **84**, 024032 (2011).

[38] A. Derdzinski, D. D’Orazio, P. Duffell, Z. Haiman, and A. MacFadyen, *Monthly Notices of the Royal Astronomical Society* **501**, 3540 (2020).

[39] A. M. Derdzinski, D. D’Orazio, P. Duffell, Z. Haiman, and A. MacFadyen, *Monthly Notices of the Royal Astronomical Society* **486**, 2754 (2019).

[40] H. Tanaka, T. Takeuchi, and W. R. Ward, *The Astrophysical Journal* **565**, 1257 (2002).

[41] H. Tanaka and W. R. Ward, *The Astrophysical Journal* **602**, 388 (2004).

[42] P. Basu, S. Chatterjee, and S. Mondal, *Monthly Notices of the Royal Astronomical Society* **531**, 1506 (2024).

[43] F. Duque, S. Kejriwal, L. Sberna, L. Speri, and J. Gair, *Phys. Rev. D* **111**, 084006 (2025).

[44] J. R. Gair, E. E. Flanagan, S. Drasco, T. Hinderer, and S. Babak, *Phys. Rev. D* **83**, 044037 (2011).

[45] E. C. Ostriker, *The Astrophysical Journal* **513**, 252 (1999).

[46] R. Fujita and W. Hikida, *Classical and Quantum Gravity* **26**, 135002 (2009).

[47] A. Pound and E. Poisson, *Phys. Rev. D* **77**, 044013 (2008).

[48] C. Cutler, D. Kennefick, and E. Poisson, *Phys. Rev. D* **50**, 3816 (1994).

[49] E. Sirko and J. Goodman, *Monthly Notices of the Royal Astronomical Society* **341**, 501 (2003).

[50] D. Gangardt, A. A. Trani, C. Bonnerot, and D. Gerosa, *Monthly Notices of the Royal Astronomical Society* **530**, 3689–3705 (2024).